ACS Catalysis

Research Article

pubs.acs.org/acscatalysis

Tuning the Electrocatalytic Water Oxidation Properties of AB_2O_4 Spinel Nanocrystals: A (Li, Mg, Zn) and B (Mn, Co) Site Variants of $LiMn_2O_4$

Clyde W. Cady,[†,§] Graeme Gardner,[†] Zachary O. Maron,[†] Maria Retuerto,[†,⊥] Yong Bok Go,[†] Shreeda Segan,[†] Martha Greenblatt,[*,†] and G. Charles Dismukes[*,†,‡]

[†]Department of Chemistry and Chemical Biology and [‡]The Waksman Institute, Rutgers University, 610 Taylor Road, Piscataway, New Jersey 08854, United States

Supporting Information

ABSTRACT: Transition metal oxides containing cubic B_4O_4 subcores are noted for their catalytic activity in water oxidation (OER). We synthesized a series of ternary spinel oxides, AB_2O_4, derived from $LiMn_2O_4$ by either replacement at the tetrahedral A site or Co substitution at the octahedral B site and measured their electrocatalytic OER activity. Atomic emission and powder X-ray diffraction confirmed spinel structure type and purity. Weak activation of the OER occurs upon A-site substitution: Zn^{2+} > Mg^{2+} > A-vacancy > Li^+ = 0. Zn and Mg substitution is accompanied by (1) B-site conversion of Mn(IV) to Mn(III), resulting in expansion and higher symmetry of the $[Mn_4O_4]^{4+}$ core relative to $LiMn_2O_4$ (inducing greater flexibility of the core and lower reorganization barrier to distortions), and (2) the electrochemical oxidation potential for Mn(III)/IV) increases by 0.15−0.2 V, producing a stronger driving force for water oxidation. Progressive replacement of Mn(III/IV) by Co(III) at the B site ($LiMn_{2-x}Co_xO_4$, $0 \le x \le 1.5$) both symmetrizes the $[Mn_{4-x}Co_xO_4]$ core and increases the oxidation potential for Co(III/IV), resulting in the highest OER activity within the spinel structure type. These observations point to two predictors of OER catalysis: (1) Among AMn_2O_4 spinels, those starting with Mn(III) in the resting lattice (prior to oxidation) result in longer, weaker Mn−O bonds for this e_g^1 antibonding electronic configuration, yielding greater core flexibility and a higher oxidation potential to Mn(IV), and (2) a linear free energy relationship exists between the electrocatalytic rate and the binding affinity of the substrate oxygen (*OH and *OOH) to the B site.

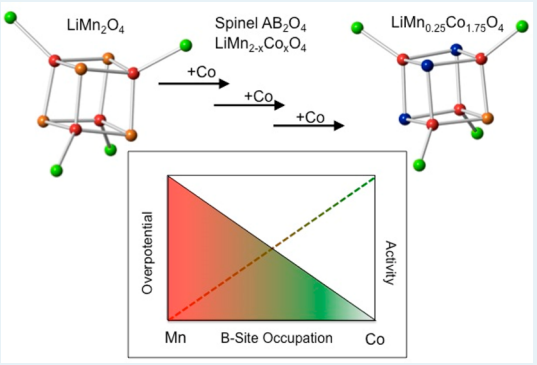

KEYWORDS: *cobalt oxide, manganese oxide, photosystem II, spinel, water oxidation catalyst, water splitting*

INTRODUCTION

Extraction of elemental hydrogen (and oxygen) from water for the production of renewable fuels is required for the long-term transition from fossil fuels and is essential for a green energy future.[1] Electrochemical cleavage of water by electrolysis is an advanced technology that is presently not competitive with fossil-generated hydrogen owing to limitations in the availability of low-cost catalyst materials, low electrochemical efficiency, and corrosion instability. The water oxidation half reaction (O_2 evolution reaction, OER) is the least efficient of the two half-cell reactions and the main focus here.

Several transition metal oxides have long been known to catalyze the OER with a marked dependence on atomic composition favoring noble metals,[2,3] whereas recent studies have elaborated on the activity of 3d-transition metal oxides.[4−8] However, fewer examples have sought to isolate the contributions from lattice structure[8−10] and electronic configuration[11,12] to OER catalysis.

OER activity correlations with structure type have shown that transition metal oxides containing cubic M_4O_4 units in both molecular[13,14] and solid state[9,10,12] compounds are more active water oxidation catalysts compared with noncubic polymorphs that are compositionally identical. Notably, spinel phase materials, AB_2O_4, with repeating cubical B_4O_4 cores are more active than layered polymorphs possessing incomplete cube B_3O_4 repeating units.[10] Among the manganese oxides, the average M−O bond length of the spinel phase is longer and therefore weaker than noncubical core types of the same oxidation state, suggesting weaker M−O(core) bonds contribute to a lower energy barrier for O_2 production among manganese spinel oxides such as $LiMn_2O_4$[13]. The longer metal−oxo bonds found in the $[M_4O_4]^{n+}$ cubical core are attributable to the greater charge density and, hence, Coulomb repulsion within the core.[15]

The OER activity among octahedrally coordinated oxides of 3d transition ions has been shown to correlate with the 3d

Received: March 1, 2015
Revised: April 22, 2015
Published: April 23, 2015

DOI: 10.1021/acscatal.5b00265
ACS Catal. 2015, 5, 3403−3410

electronic configuration. Specifically, comparison among eight crystalline manganese oxides of different oxidation state and structure types established a direct correlation between OER activity and content of Mn(III) across three different lattice structure types.[12] With its high spin electronic configuration, $t_{2g}^3e_g^1$, the antibonding e_g electron in the valence $3d_{z2}$ orbital creates two long Mn−O bonds that are weaker in energy. Analogously, among an isostructural family of perovskite oxides (ABO_3), an occupancy of one electron in the degenerate antibonding 3d orbitals (e_g^1 in cubic symmetry) on atom B was shown to correlate with higher OER activity among a series of B-site substitutions.[11]

Theoretical analysis of the perovskite series has predicted a volcano correlation between the overpotential for the OER reaction and the standard free energy difference for oxidation of absorbed hydroxyl bound to the surface (*), eq 1:[16]

$$HO^* \rightarrow O^* + H^+ + e^- \quad (1)$$

Taken together, the experimental and theoretical studies point to an optimal balance between M−O* (substrate) and M−O (core) bond strengths for OER activity. The evidence suggests that this can best be achieved when the B metal with octahedral coordination has full bond order to M−O* (substrate) and partial antibonding character to M−O (core), corresponding to valence d electronic configurations e_g^1.

Herein, we extend this study of the influence of electronic configuration on OER activity by replacing the B-site Mn(III) ions of the spinel $LiMn_2O_4$ (AB_2O_4) with one, two, or three Co(III) ions per B_4O_4 cube. By fixing the spinel structure type, the influence of B-site electronic configuration on the OER activity has been isolated. The larger nuclear charge ($\Delta Z = +2$) and low-spin electronic configuration of Co(III), $(t_{2g})^6$, vs the high-spin configuration of Mn(III), $(t_{2g})^3(e_g)^1$, provides an increase in the charge density, creates a more symmetrical ligand field, and eliminates the antibonding e_g^1 electron, resulting in increased M−O (core) bond strength. We also investigate the dependence of OER activity on substitution of the A-site Li^+ cation by Mg^{2+} and Zn^{2+} in spinel AMn_2O_4, which results in increasing the Mn−O (core) bond energy. Last, we apply this knowledge to better understand how water oxidation may occur in natural oxygenic photosynthetic organisms by photosystem II (PSII) enzymes.

EXPERIMENTAL SECTION

Synthesis of nanoparticles of the spinels was accomplished by application of the low temperature sol−gel method used for $LiMn_2O_4$.[9] For example, $LiMnCoO_4$ was synthesized by dissolving $MnOAc_2{\cdot}4(H_2O)$ (2.5 mmol, 0.610g) (where OAc = acetate), $LiOAc{\cdot}2(H_2O)$ (2.5 mmol, 0.255g), $CoOAc_2{\cdot}4(H_2O)$ (2.5 mmol, 0.622g), citric acid (15 mmol, 2.88g), and urea (15 mmol, 0.90g) with 20 mL of water and 2 mL of nitric acid in a beaker. The solution was heated to 80 °C while stirring until enough water had evaporated to create a gel. The gel was then dried at 170 °C overnight to remove the remaining water and then calcined at 350 °C for 6 h. This method produces monophasic $LiMnCoO_4$ free of other phases, as determined by powder X-ray diffraction (PXRD) and elemental analysis (see SI). Unless otherwise stated, analytical reagent grade chemicals were purchased from Sigma-Aldrich and used as received.

$ZnMn_2O_4$ was synthesized by replacing LiOAc with $Zn(NO_3)_2$. $MnOAc_2{\cdot}4(H_2O)$ (5 mmol, 1.22g), $Zn(NO_3)_2{\cdot}6(H_2O)$ (2.5 mmol, 0.744g), citric acid (15 mmol, 2.88g), and urea (15 mmol, 0.90g) were dissolved in ultrapure water (~20 mL) and 2 mL of nitric acid and were treated in a manner analogous to the lithium spinel. $MgMn_2O_4$ was synthesized analogously by replacing LiOAc with $Mg(NO_3)_2$.

All products were initially characterized by PXRD (Cu $K\lambda$ = 1.5406 Å) on a Bruker D8 Advance diffractometer for phase identification, phase purity, and structural characterization. The structures were refined by the Rietveld method,[17] with the Fullprof refinement program.[18] In the final run, the scale factor, background coefficients, unit-cell parameters, and positional coordinates were refined.

Catalyst-ionomer films were fabricated by modifying a standard published procedure,[10,11] starting with a solution consisting of 5 mg of catalyst and 1.5 mg of nanoparticulate carbon (Acetlyene Black; 50% compressed) in 0.5 mL neutral Nafion (2 parts 5% Nafion solution mixed with 1 part 0.1 M NaOH). Briefly, the solution was sonicated for 10 min to disperse the particles evenly and, 3 μL was drop-cast on the glassy carbon electrode. The solution was allowed to evaporate on the benchtop for 1 h and then dried at 120 °C for 20 min to remove any remaining water. The electrochemical current from these catalyst-film electrodes was normalized to the geometric area while maintaining a constant weight loading of the catalyst and catalyst-to-carbon ratio.

Electrochemical measurements were carried out with a CH Instruments electrochemical workstation model CHI 700C and a three-electrode cell consisting of a 5 mm diameter glassy carbon working electrode, a Ag/AgCl (3.5 M KCl) or Hg/HgO (1 M NaOH) reference electrode, and a platinum wire or carbon rod counter electrode. Standard cyclic voltammetry measurements were carried out at a sweep rate of 100 mV/s, and slow scan CVs to obtain kinetic data were carried out at 10 mV/s. The steady-state current due to water oxidation in neutral pH (0.1 M phosphate) was determined by measuring the current after holding a constant potential, 1.2 V vs Ag/AgCl, for 10 min in a vigorously stirred solution (chosen to allow direct comparison to previous experiments).[11] This incubation period allowed capacitance transients to dissipate and preoxidation of the catalyst to occur and produced a stable steady-state current, as shown in Supporting Information Figure S1. Electrocatalytic activity of the catalysts was also measured in alkaline conditions (1 M NaOH), where activity is greatly enhanced and kinetic features like Tafel slope can be probed more easily. Scan-rate dependence of the nonfaradic capacitance of the different samples in the B-site substituted series was also examined to determine a relative trend in electrochemical surface area. Capacitance values obtained were used only to make relative comparisons, and absolute numbers for the surface area are not reported, given the assumptions used for this type of analysis.[19]

Gaseous products were identified by gas chromatography following transfer from the headspace of the cell via gastight syringe.

RESULTS

Particle Size. The size, morphology, and surface area of the synthesized particles was investigated by three approaches: scanning electron microscopy (Zeiss Sigma FESEM), PXRD, and capacitance measurements by electrochemical impedance spectroscopy (ECIS).

FESEM. Representative field emission SEM images of materials in the series are given in Figure 1. All samples exhibit polydispersed morphology with a high degree of particle

DOI: 10.1021/acscatal.5b00265
ACS Catal. 2015, 5, 3403−3410

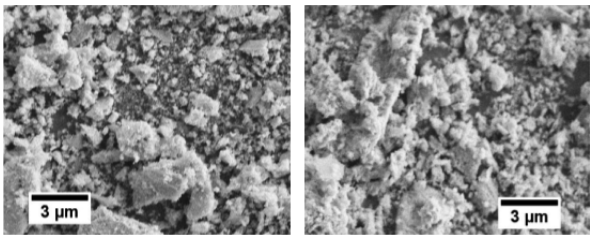

Figure 1. SEM images of $LiMn_{1.5}Co_{0.5}O_4$ (left) and $LiMn_{0.5}Co_{1.5}O_4$ (right) illustrating the similar morphology for both samples within the series.

agglomeration consisting of individual crystallites in the size range 20−100 nm using a synthesis temperature of 350 °C and 6 h calcination time.[9,20] The lower limit of the crystallite size agrees well with our results from PXRD (20−30 nm), as described in the next section.

ECIS. Capacitance measurements were performed to determine the effect of the catalyst layer by application of an applied electrical polarization. This method was investigated by the scan-rate dependence of the nonfaradic current at electrochemically inactive potential.[3] The current I_{dl} vs scan rate plot was used to obtain the value of the charging capacitance, C_{dl}, from a linear fit of the data. We normalized this value to the geometric area of the underlying glassy carbon electrode to get relative numbers for the mixed Mn/Co B-site series, presented in Supporting Information Table S1. C_{dl} is particularly useful for estimating the volume of the catalyst layer that can be charged or changes in its relative surface area in contact with the electrolyte. We observe an 8-fold linear increase in the normalized capacitance values with increasing Co content in the B site. The effect this trend has on catalytic activity will be discussed later.

PXRD. B-Site Substitution. Our goal was to substitute Co selectively in the B site of $LiMn_2O_4$ to produce a range of ternary Mn/Co spinels (ideally $LiMn_{2-x}Co_xO_4$, x = 0−2) without displacing Li from the A site and without forming other phases (i.e., Co_3O_4 or $LiCoO_2$). To do this, we started with our previously reported synthesis of nanoparticulate $LiMn_2O_4$ and varied the initial molar ratio of Co/Mn in the synthesis reagents for x = 0−1.75 in 0.25 increments while monitoring both PXRD and elemental composition (ICP-OES). The PXRD in Figure 2 confirmed the formation of the spinel structural phase for x = 0−1.75 with the expected decrease in the cell parameters (Figure 2, insert) due to the smaller effective ionic radius of Co(III) (0.545 Å) as it replaces Mn(III)(0.645 Å).[21] Above 1.75 Co/Mn loading, PXRD revealed two new features indicating formation of both $LiCoO_2$ and Co_3O_4 as separate phases, and this sample therefore was not examined further. Within the range $1.00 \leq x \leq 1.75$, PXRD revealed that minority reflections appear at 2θ = 32° and 56° that are not identical to either $LiMn_2O_4$ or $LiCoO_2$ (arrows in Figure 2). The origin of these reflections was estimated as described below.

We used $LiMn_2O_4$ as the starting point to refine the structure. In this cubic structure, Li atoms are situated at A (1/4 1/4 1/4) positions, with 8*a* multiplicity (tetrahedral position); Mn atoms at B (1/2 1/2 1/2) with 16*d* multiplicity (octahedral positions); and O atoms at (x x x) with 32*e* multiplicity. The small peaks appearing at 2θ = 32° and 56° at $x \geq 1$ (Figure 2, arrows) are consistent with either manganese or cobalt partially replacing lithium in the tetrahedral A-site position at (1/4 1/4 1/4) on the basis of simulation of the PXRD structures (see

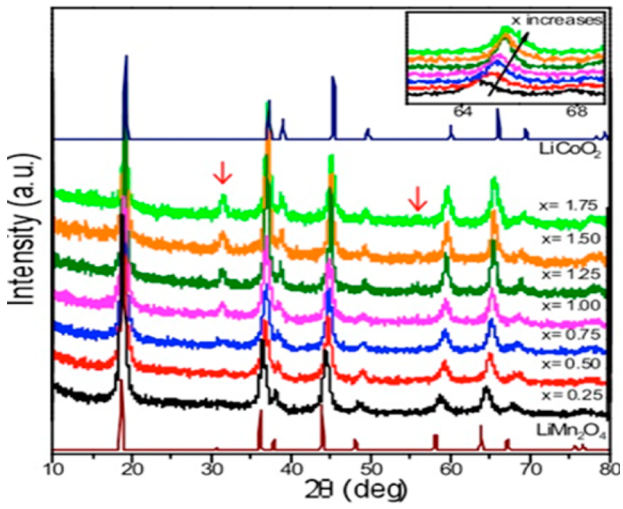

Figure 2. Powder X-ray diffraction series of seven synthesized nanoparticulate spinel complexes of composition $LiMn_{2-x}Co_xO_4$, x = 0.25−1.75. Reference spectra for polycrystalline $LiMn_2O_4$ and cubic $LiCoO_2$ are shown in brown (bottom) and blue (top), respectively. The inset illustrates the shift to a smaller lattice parameter with higher cobalt content.

Supporting Information, Figure S3) and comparison with the reference PXRD of spinel Co_3O_4. Because PXRD cannot distinguish accurately between Mn and Co occupation in the Li position, only their combined occupation probability could be assigned from the peak intensity. However, because these features grow in intensity with increasing Co (x) content, the PXRD shows that as x increases above 1, Co or Mn partially occupies the tetrahedral A sites by displacement of Li, as previously reported.[22]

Because of the similarity of X-ray scattering by Co and Mn and the broad PXRD peaks, it is difficult to assign the Co/Mn ratio in the B sites by PXRD alone. To resolve this question, we measured the content of Mn and Co by atomic emission spectroscopy (ICP-OES). Figure 3 plots the Co and Mn content measured by ICP-OES versus the expected composi-

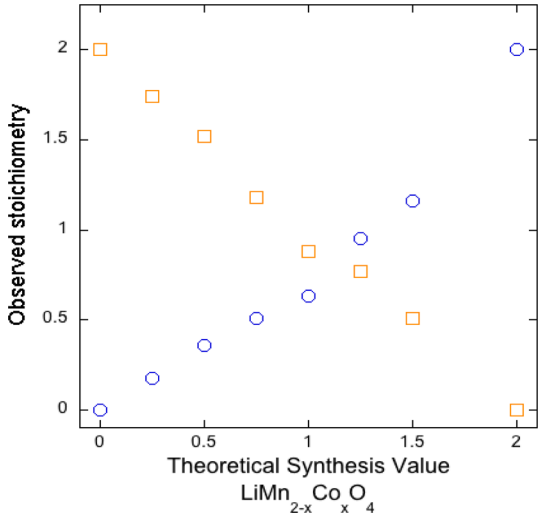

Figure 3. Measured molar content of Mn and Co in the isolated product based on weight of product vs the molar ratio based on weight of reactants used for synthesis; Mn (□), Co (○) were obtained from ICP-OES analysis.

DOI: 10.1021/acscatal.5b00265
ACS Catal. 2015, 5, 3403−3410

tion on the basis of synthesis stoichiometry. A monotonic inverse relationship between manganese and cobalt content is observed, albeit with different slopes, suggesting partial A-site occupation by Co as x increases.

The Co/Mn ratio measured by ICP-OES and the A-site Co + Mn occupancy as measured by PXRD were used to obtain a quantitative Co/Mn ratio in the B site (Table 1). The

Table 1. Calculated Average Stoichiometries from the Structural Refinements by the PXRD Data Sets Constrained by the Experimental Stoichiometries Determined by ICP-OES

as synthesized	Mn/Co	calcd stoichiometry
$LiMn_{1.75}Co_{0.25}O_4$	9.9	$LiMn_{1.8(3)}Co_{0.18(3)}O_4$
$LiMn_{1.50}Co_{0.50}O_4$	4.2	$LiMn_{1.62(2)}Co_{0.38(2)}O_4$
$LiMn_{1.25}Co_{0.75}O_4$	2.3	$(LiCo_{0.15(3)})(Mn_{1.50(3)}Co_{0.45(3)})O_4$
$LiMn_{1.0}Co_{1.0}O_4$	1.3	$(LiCo_{0.22(1)})(Mn_{1.28(1)}Co_{0.72(1)})O_4$
$LiMn_{0.75}Co_{1.25}O_4$	0.80	$(LiCo_{0.25(3)})(Mn_{1.00(3)}Co_{1.00(3)})O_4$
$LiMn_{0.50}Co_{1.50}O_4$	0.44	$(LiCo_{0.34(1)})(Mn_{0.71(1)}Co_{1.29(1)})O_4$

Supporting Information gives the PXRD fittings compared with the appropriate standards. The fittings show that Co occupation of the A site has the compositions listed in Table 1 for the six mixed Mn/Co samples. For the sake of clarity in this paper, we refer to all the compositions by the synthesis formula.

Electrochemical Measurements. As noted above, the particle sizes of the six Co B-site catalysts listed in Table 1 are indistinguishable by both SEM and peak-broadening in PXRD. Hence, the surface area in contact with the solution is expected to be the same for all of the samples. For this reason, the catalyst mass loading was kept the same in all cases (~300 μg cm^{-2} electrode).

Film electrodes with a high manganese content show a precatalytic oxidation at 850 mV vs Ag/AgCl due to Mn(III) oxidation.[9] Cyclic voltammograms (CVs) of representative Mn/Co samples are shown in Figure S5. Samples with either high Co content, above $x \geq 1.5$, or low Co content, below $x < 0.5$, prominently exhibit this precatalytic shoulder for Mn(III) at approximately the same potential range. The observed oxidation peak in these samples occurs at 0.85−0.90 V (Figure S5 and S6), whereas samples with approximately equal Mn and Co content show no precatalytic feature. It is reasonable to conclude that this trend is due to Co(III) selectively replacing Mn(III) in the mixed-valent $LiMn_2O_4$, yielding $LiMn(IV)Co(III)O_4$, as expected.

The results of the cyclic voltammetry experiments in alkali (pH 14) are shown in Figure 4. The baseline trace for $LiMn_2O_4$ is equal to the spinel-free baseline (no OER), as we previously reported.[9,10,12] Within the series of Co-substituted $LiMn_2O_4$ spinel, we see one very distinct trend and one that is more subtle. The dominant trend seen is that replacement of Mn by Co causes an obvious increase in the current density at high overpotentials proportional to the Co content (x = 0−1.75). At the higher Co concentrations, x = 1.5−1.75, the formation of a minor Co_3O_4 impurity (Figure 2) may contribute to the electrochemical response. The second (subtle) trend seen in Figure 4 is that the manganese-rich spinels have an earlier onset potential, provided they contain some cobalt, x = 0.33−1. Both of these trends are illustrated by comparing the Tafel slope and the overpotential (we chose 1 mA current density) as a function of the Co B-site occupancy depicted in Figure 5. As

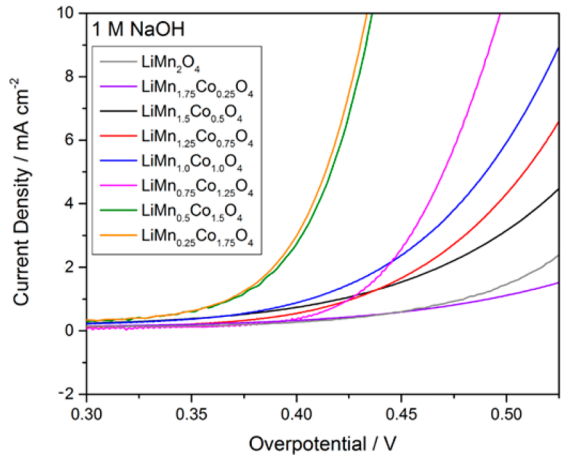

Figure 4. Polarization curves showing OER activity of the $LiMn_{2-x}Co_xO_4$ series at pH 14 (1 M NaOH).

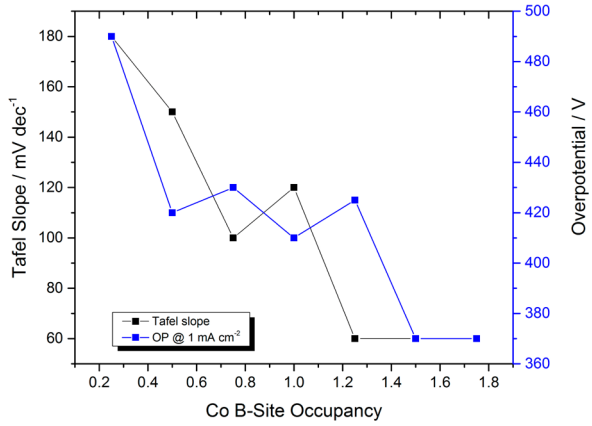

Figure 5. Plot showing Tafel slope and overpotential (at 1 mA cm^{-2}) with increasing cobalt B-site occupancy. pH = 14 at 1 M NaOH.

the initial Co content increases, both the Tafel slope and the overpotential decrease, followed by a discontinuity at roughly 1:1 Co/Mn and then decrease to a minimum at and above 1.5 Co. The Co-rich spinel phase exhibits a lower Tafel slope of 60 mV dec^{-1} (3-fold lower) and lower overpotential of 370 mV (120 mV lower at 1 mA/cm^2).

The OER catalytic current at 1.2 V applied potential (~600 mV overpotential) in a buffered solution at pH 7 is plotted in Figure 6. This plot and the corresponding data at pH 14 (Figure 4) establish linear dependences of the OER activity on Co B-site content at pH 7 and 14, respectively.

A-Site Substitution. In a previous report, we showed that >90% removal of Li^+ from $LiMn_2O_4$ to form the λ-MnO_2 transforms the inactive material to a low-activity water oxidation catalyst.[9] To test the source of this change, we substituted Zn and Mg for Li ions in the A site of $LiMn_2O_4$ using the same sol−gel synthesis procedure adapted to produce the previously reported spinels.[23,24]

PXRD: A Site. The PXRD patterns for both the Zn and Mg derivatives produced excellent fits to the calculated patterns, confirming retention of the spinel structure type with occupation of A sites by Zn and Mg (Figure S4). Table 2 shows that when Li is substituted by Zn or Mg, the average Mn_4O_4 cube dimensions increase and the Mn_4O_4 cube distorts less, becoming a more regular cubic symmetry. Although the effective ionic radii are similar for Li(I)(0.59 Å), Mg(II)(0.57

DOI: 10.1021/acscatal.5b00265
ACS Catal. 2015, 5, 3403−3410

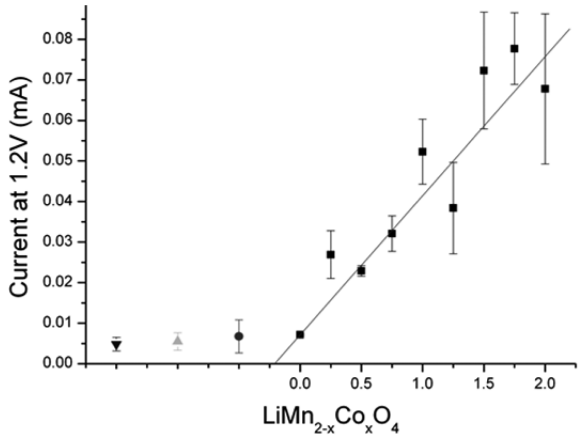

Figure 6. Dependence of the steady-state electrocatalytic current on the B-site Co content in $LiMn_{2-x}Co_xO_4$ (squares). Left side of graph shows various controls: plain glassy carbon electrode (●), Nafion on glassy carbon (▲), and Nafion + acetylene black on glassy carbon (▼). The applied potential is 1.2 V vs Ag/AgCl (3.5 M KCl) at pH = 7. Data are the mean of three measurements on separate samples with standard error shown.

Å), and Zn(II)(0.6 Å), these substitutions require replacement of the Mn(IV) with Mn(III) to maintain charge neutrality. As expected, the average Mn−O bond lengths are longer compared with the Li derivative (ΔR = 0.108 and 0.063 Å for Mg and Zn, respectively). This occurs owing to the complete replacement of Mn(IV) with Mn(III) with its antibonding e_g^1 electron. Consequently, each of the four Mn(III) has two different Mn−O bond lengths with local tetragonal geometry, as is typical of Jahn−Teller elongated ions with e_g^1 (d_{z2}^1) electronic configuration. Table 2 also shows that the Mn_4O_4 cube becomes more symmetrical as the internal angles approach 90° in both the Mg and Zn derivatives. We conclude that the longer and weaker Mn−O bond and bond angle bending modes in both the Mg and Zn derivatives are weaker and more flexible to displacements, both key variables for OER catalysis.

Figure 7 compares linear sweep voltammetry of a selection of the electrodes described in this report. A significant preoxidation feature is observed for the AMn_2O_4 (A = Mg, Zn) samples, which confirms the increased content of Mn(III) relative to Mn(IV) in these materials. The $MgMn_2O_4$ sample shows a weaker and broader Mn(III) preoxidation feature in both the linear sweep scan and the CV (Figure S6). Comparison of the potentials that produce the peak oxidation current for Mn(III) → Mn(IV) in the CV experiment (Figure S5) reveals that Mg and Zn substitution at the A site increases the oxidation potential by 0.15−0.2 V relative to $LiMn_2O_4$.

Figure 7 shows that at higher oxidation potentials above the preoxidation feature (>1.2 V), the Zn and Mg derivatives have

Table 2. Structure and Relative OER Current of Spinel Type Cubic Metal Oxides[a]

Metal Oxide	Side view -	Top view	Cube Mn-O Distance (Å)	OER Current at 1.2V (10^{-5}A)	Structure Ref.
$LiMn_2O_4$		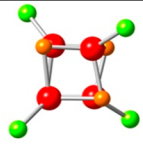	1.887 2.106 2.067 2.035 1.998	< 0.71	[30]
λ-MnO_2 <10% Li^+			1.910	1.8	[31]
$MgMn_2O_4$			1.978 2.275	2.9	[24]
$ZnMn_2O_4$		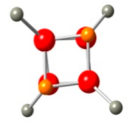	1.952 2.211	4.0	[23]
Co_3O_4	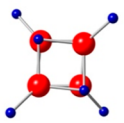		1.921	4.1	[23]
cubic-$LiCoO_2$	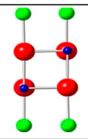		1.969	5.2	[32]
1. Steady-state OER current measured after 10 minutes at 1.2V vs Ag/AgCl in 0.1 M phosphate buffer pH = 7					

[a]Li (green), O (red), Mn (orange), Co (blue), Mg (yellow), Zn (grey).

DOI: 10.1021/acscatal.5b00265
ACS Catal. 2015, 5, 3403−3410

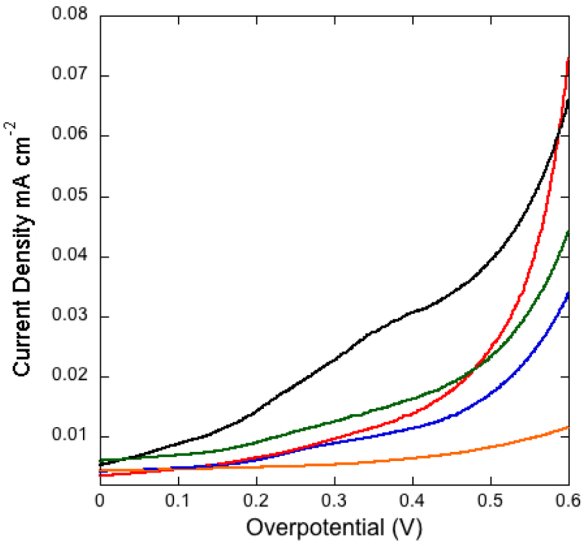

Figure 7. Linear sweep voltammetry of Nafion film electrodes containing $LiMnCoO_4$ (red), $ZnMn_2O_4$ (black), $MgMn_2O_4$ (green), λ-MnO_2 (blue), and blank glassy carbon (orange). $LiMn_2O_4$ is indistinguishable from thr blank. Electrochemistry was carried out vs saturated Ag/AgCl in 0.1 M phosphate buffer pH 7, scan rate of 5 mV/s with constant stirring.

greater OER activity when compared with the λ-MnO_2 sample, but significantly less activity than the ternary spinel $LiMnCoO_4$ containing 50% Co(III) and 50% Mn(IV) in the B site. We have refined the possible disorder between the cations over both the tetrahedral and octahedral positions in AMn_2O_4 and determined that a small disorder, ~4% and ~9%, of Mn occupy the Mg and Zn tetrahedral sites, respectively. A corresponding disorder of Mg and Zn, respectively, on the octahedral Mn site is also observed (see SI). This disorder could account for some of the differences in activity between the Mg and Zn compounds.

DISCUSSION

A Site OER Dependence. The order of steady-state OER current densities for A-site spinels in AMn_2O_4 is Zn ~ Mg > λ > Li. We dismiss hydrolysis of water bound to a surface A-site cation as a possible contributor to the catalytic OER current at pH 7 because there is no obvious trend with Lewis acidities (Zn^{2+} > Mg^{2+} > Li^+). Indeed, $LiMn_2O_4$ is inactive, whereas the A-site vacancy in λ-MnO_2 gives rise to measurable OER activity.[9] This is not unexpected, considering that all three cations have pK_a values well above the solution pH, and so neutral water ligands, not hydroxide ligands, would be present. The oxidation potential of Mn(III) increases from Li to Mg to Zn by 0.15 and 0.20 V, respectively. In solid state terminology, the valence band potential shifts positively by 0.15−0.2 V. This shift is consistent with the expected trend of greater A−O bond strength for these divalent cations. Correspondingly, the Mn−O bond strength and covalency decrease in this same order.[25] The resulting weaker ligand field strength at Mn is a principal cause of the higher oxidation potential, owing to the greater destabilization of Mn(IV) relative to Mn(III). The Zn and Mg derivatives follow the same e_g^1 trend observed for the perovskite oxides[11] and other structurally distinct manganese oxides (Mn_2O_3 and Mn_3O_4).[12]

Our results indicate that both redox energy differences (greater Mn(IV) reduction potential) and weaker vibronic distortion energies (longer Mn−O bonds and flexible cube modes) contribute to the faster OER kinetics for the Mg and Zn derivatives. The greater Mn(IV) reduction potential will contribute to faster kinetics because this directly increases the driving force for surface water oxidation. The rate of regeneration of Mn(III) in the penultimate step of the catalytic cycle before O_2 release (denoted the reductive phase herein; see Scheme 1) may contribute to the higher catalytic activity of

Scheme 1. A Proposed Mechanism for Catalytic Water Oxidation by AB_2O_4 Spinel Oxides[a]

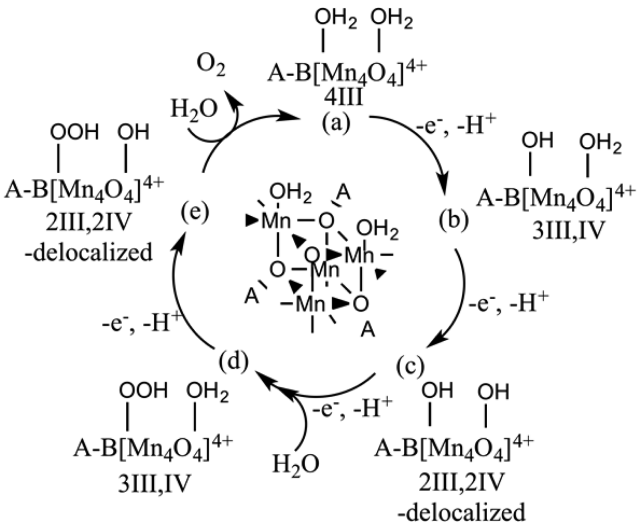

[a]B-site cube denoted as $B[Mn_4O_4]^{n+}$ with formal charge n+ = 4+ indicated to allow assignment of Mn oxidation states given in Roman numerals. Central image illustrates intermediate a. (a) "diaquo", A sites = Zn^{2+}, Mg^{2+}, starting oxidation state for $ZnMn_2O_4$ and $MgMn_2O_4$. (b) "aquo-hydroxo", B-site valence e_g^1 electrons are delocalized in this mixed valence state. (c)"dihydroxo", A sites = Li^+, starting oxidation state for $LiMn_2O_4$ and $Li(CoMn)O_4$. (d) "aquo-hydroperoxo". (e) "hydroxo-hydroperoxo", B-site valence e_g^1 electrons are delocalized in this mixed valence state.

the Mg and Zn derivatives. Their longer Mn−O bonds result in weaker Jahn−Teller trapping energy, resulting in a lower nuclear reorganization barrier, as predicted by kinetic theory.[26] For example, the unconstrained $[Mn(III)F_6]^{3-}$ anion exhibits a J-T trapping energy of 1 eV for pseudorotation of the tetragonal distortion axis between the three equivalent positions.[25] Complexes of $Mn(III)(OR)_6$ have comparable J-T bond distortions as $[Mn(III)F_6]^{3-}$ and, thus, are expected to have similar trapping energies. These considerations are applied in our proposed mechanism for water oxidation given in Scheme 1.

Different physical properties among the Co B-site derivatives that could potentially contribute to the different OER currents will be considered next: (1) electrical conductivity/capacitance, (2) the oxidation potential of the B-site ion, (3) the electronic configuration of the B-site ion, and (4) the metrical structure/flexibility of the Mn_4O_4 subcore.

B-Site OER Dependence. Many variables can potentially contribute to the electrical current in electrocatalysis experiments: the number of catalytic sites, their intrinsic catalytic activity, their accessibility to both a continuous supply of water substrate, and the conducting pathways for electrons to the electrode and protons to the electrolyte. We observe that the charging capacitance increases linearly with increasing cobalt

DOI: 10.1021/acscatal.5b00265
ACS Catal. 2015, 5, 3403−3410

content in the B site, suggesting that at least in part, the activity increase could be due to the presence of more electrochemically accessible sites—meaning either greater active surface area in contact with polarizable electrolyte or greater electrical access to more material while maintaining the same surface area. Only the former change can contribute to a sustained catalytic current. Because the spinel phase, catalyst particle size, loading, and film thickness were constant in our experiments, we attribute the greater charging capacitance at noncatalytic potentials to the higher electrical conductivity of the Co-rich phase materials (larger charging volume). With this result, we can attribute the increase in the sustained current density above the OER potential for Co vs Mn spinel phase to the greater intrinsic catalytic activity.

When comparing the Mn−O and Co−O bond lengths in Table 2, it is apparent that Co(III) in the B site of Co_3O_4 spinel has significantly shorter M−O bonds than those with Mn(III). The loss of the Mn(III) preoxidation feature in cyclic voltammetry of the mixed Mn/Co spinels ($x \geq 1$) reveals that the smaller Co(III) ion replaces Mn(III) instead of Mn(IV). The higher affinity for Co(III) arises from its low-spin electronic configuration, $3d^6$ $(t_{2g})^6$, which has no antibonding e_g electrons, in contrast to the high-spin configuration Mn(III), $3d^4$ $(t_{2g})^3(e_g)^1$. This greater Co(IIII)−O bond strength as a descriptor of relative OER catalytic rate is in agreement with theoretical[27] and experimental[3] observations covering a wide range of oxides, electrodeposited cobalt phosphate films,[28] and the perovskite oxides.[16]

CONCLUSIONS AND PROPOSED MECHANISM

In summary, two distinct predictors of OER catalytic rate are implicated from the present studies of substituted spinel oxides: (1) substrate oxygen (*O) bond strength at the cubic M_4O_4 B site, and (2) occupancy of the e_g^1 electronic configuration at the B site. 3d Metal oxides with a single occupancy of the antibonding e_g^1 electronic configuration provide a distorted lattice structure that stabilizes this configuration relative to more reduced or oxidized ones (Table 2). Consequently, oxidized Mn(IV) ions with e_g^0 electron counts pay an energy penalty to form in e_g^1 lattices. This redox energy destabilization indicates a deeper e_g orbital energy, which is precisely what is needed to more strongly interact with the bonding orbital of the substrate hydroxide/oxide, resulting in faster OER kinetics.

We put these two concepts together in a proposed mechanism, given in Scheme 1, that attempts to explain the chemical basis for the dependence of water oxidation efficiency at the B site of spinel oxides. This mechanism is supported also by theoretical calculations of the isolated cubical Co_4O_4 core type.[29]

Reduction of Mn(IV) occurs in two steps in the catalytic cycle in which terminally bound substrate water molecules are oxidized to form a "hydroperoxo" intermediate and O_2 product, respectively (Scheme 1 reactions: c → d and e → a). These reaction types are believed to be responsible for the observed dependence of the OER catalytic rate for other manganese oxides (Mn_2O_3, Mn_3O_4 and λ-MnO_2)[12] and for the e_g^1 type perovskite oxides.[11] For these materials, the B-site content of the e_g^1 configuration ion directly correlates with the catalytic rate. For the Mg and Zn A-site derivatives reported here, the B site of these (as isolated) spinels is exclusively Mn(III) and, thus, has the maximum e_g^1 population. The same correlation with catalytic activity is evident with the Mg and Zn A-site derivatives. However, there is another likely contribution to the rate arising from the 0.15−0.2 V increase in the oxidation potential of the B-site Mn(III)/Mn(IV) in these compounds relative to the Li derivative (Figure S5 and Figure S6). Structurally, there is reduced O (core) → Mn interaction in Zn(Mg) derivatives, resulting in a higher energy of the 3d valence orbitals. This causes them to be radially more extended[25] and could therefore overlap better with surface-bound water molecules. The stronger Mn−O (substrate) bonds could be responsible for the observed faster OER rate and are predicted to accelerate one or more of the following reactions (Scheme 1): a → b, b → c, and d → e, all of which involve formation of either hydoxo or hydroperoxo substrate intermediates bound to Mn ions.

Substitution of Co(III) for Mn(III) at B sites eliminates the e_g^1 electron effect but increases the reduction potential for the Co(IV)/Co(III) couple by 100 mV relative to the Mn(IV)/Mn(III) couple in Li spinel-type oxides (see Figure S6). In addition, the Pourbaix diagrams for Mn and Co aqua species clearly illustrate that Mn(IV) has greater stability.[33] This higher reduction potential may contribute to the faster observed OER rate for the Co derivatives.

The foregoing analysis is in agreement with theoretical predictions[27] and experimental observations[3] covering a wide range of oxides that show that the binding affinity of the substrate hydroxo and hydroperoxo intermediates are linear predictors of the catalytic OER rate. According to these correlations, the experimental binding energy of the hydroperoxo bond (HOO*) is weaker than the corresponding hydroxo bond (HO*) by a constant 3.2 ± 0.4 eV (95% CL) for a wide range of oxides (perovskites, rutiles, Mn_xO_y, and anatase).[26]

The foregoing discussion of the energetics of the ideal catalyst applies to both the forward and reverse reactions and thus does not explain the preferred directionality of the catalytic cycle. This can be introduced by coupling the steps to irreversible processes (entropy), such as the release of protons into the medium, either by dilution or use of buffers, and by removal of the O_2 product. These entropic terms will accelerate the forward steps of the cycle in a manner that is readily testable using pH buffers of different capacities or pK_a and by varying the O_2 partial pressure.

ASSOCIATED CONTENT

Supporting Information

Supporting Information contains experimental details for fitting PXRD and cyclic voltammetry **Figure**s S1 to S8 This material is available free of charge via the Internet at http://pubs.acs.orgThe Supporting Information is available free of charge on the ACS Publications website at DOI: 10.1021/acscatal.5b00265.

AUTHOR INFORMATION

Corresponding Authors

*E-mail: dismukes@chem.rutgers.edu.

*E-mail: martha@chem.rutgers.edu.

Present Addresses

§(C.W.C.) Department of Chemistry, University of Connecticut, Storrs, CT.

⊥(M.R.) Niels Bohr Institute, University of Copenhagen, DK-2100 Copenhagen, Denmark.

Notes

The authors declare no competing financial interest.

DOI: 10.1021/acscatal.5b00265
ACS Catal. 2015, 5, 3403−3410

■ ACKNOWLEDGMENTS

We thank Paul Smith for discussions. This work was funded by AFOSR grant FA9550-11-1-0231 and a postdoctoral fellowship supported by NATCO Pharma.

■ REFERENCES

(1) Faunce, T. A.; Lubitz, W.; Rutherford, A. W.; MacFarlane, D.; Moore, G. F.; Yang, P.; Nocera, D. G.; Moore, T. A.; Gregory, D. H.; Fukuzumi, S.; Yoon, K. B.; Armstrong, F. A.; Wasielewski, M. R.; Styring, S. *Energy Environ. Sci.* **2013**, *6*, 695−698.
(2) Harriman, A.; Pickering, I. J.; Thomas, J. M. *J. Chem. Soc., Faraday Trans. 1* **1988**, *84*, 2795−2806.
(3) Bockris, J. O.; Otagawa, T. *J. Electrochem. Soc.* **1984**, *131*, 290.
(4) Kikuchi, T.; Tanaka, K. *Eur. J. Inorg. Chem.* **2014**, *2014*, 607−618.
(5) Fukuzumi, S.; Hong, D. *Eur. J. Inorg. Chem.* **2014**, *2014*, 645−659.
(6) Swierk, J. R.; Mallouk, T. E. *Chem. Soc. Rev.* **2013**, *42*, 2357−2387.
(7) Maitra, U.; Naidu, B. S.; Govindaraj, A.; Rao, C. N. R. *Proc. Natl. Acad. Sci. U. S. A.* **2013**, *110* (29), 11704−11707.
(8) Gerken, J. B.; McAlpin, J. G.; Chen, J. Y. C.; Rigsby, M. L.; Casey, W. H.; Britt, R. D.; Stahl, S. S. *J. Am. Chem. Soc.* **2011**, *133*, 14431−14442.
(9) Robinson, D. M.; Go, Y. B.; Greenblatt, M.; Dismukes, G. C. *J. Am. Chem. Soc.* **2010**, *132*, 11467−11469.
(10) Gardner, G. P.; Go, Y. B.; Robinson, D. M.; Smith, P. F.; Hadermann, J.; Abakumov, A.; Greenblatt, M.; Dismukes, G. C. *Angew. Chem., Int. Ed.* **2012**, *51*, 1616−1619.
(11) Suntivich, J.; May, K. J.; Gasteiger, H. A.; Goodenough, J. B.; Shao-Horn, Y. *Science* **2011**, *334*, 1383−1385.
(12) Robinson, D. M.; Go, Y. B.; Mui, M.; Gardner, G.; Zhang, Z.; Mastrogiovanni, D.; Garfunkel, E.; Li, J.; Greenblatt, M.; Dismukes, G. C. *J. Am. Chem. Soc.* **2013**, *135*, 3494−3501.
(13) Brimblecombe, R.; Koo, A.; Dismukes, G. C.; Swiegers, G. F.; Spiccia, L. *J. Am. Chem. Soc.* **2010**, *132*, 2892−2894.
(14) Smith, P. F.; Kaplan, C.; Sheats, J. E.; Robinson, D. M.; McCool, N. S.; Mezle, N.; Dismukes, G. C. *Inorg. Chem.* **2014**, *53*, 2113−2121.
(15) Dismukes, G. C.; Brimblecombe, R.; Felton, G. A. N.; Pryadun, R. S.; Sheats, J. E.; Spiccia, L. *Acc. Chem. Res.* **2009**, *42*, 1935−1943.
(16) Garcia-Mota, M.; Vojvodic, A.; Metiu, H.; Man, I. C.; Su, H. Y.; Rossmeisl, J.; Norskov, J. K. *ChemCatChem* **2011**, *3*, 1607−1611.
(17) Rietveld, H. M. *J. Appl. Crystallogr.* **1969**, *2*, 65−71.
(18) Rodriguez-Carvajal, J. *Phys. B* **1993**, *192*, 55−69.
(19) Trasatti, S.; Petrii, O. A. *Pure Appl. Chem.* **1991**, *63*, 711−734.
(20) Vivekanandhan, S.; Venkateswarlu, M.; Satyanarayana, N. *J. Alloys Compd.* **2007**, *441*, 284−290.
(21) Shannon, R. D. *Acta Crystallogr., Sect. A: Cryst. Phys., Diffr., Theor. Gen. Crystallogr.* **1976**, *A32*, 751−767.
(22) Jiao, F.; Frei, H. *Angew. Chem., Int. Ed.* **2009**, *48*, 1841−1844.
(23) Nogues, M.; Poix, P. *C.R. Acad. Sci. Series C* **1971**, *272*, 1318−1320.
(24) Radhakrishnan, N. K.; Biswas, A. B. *Zeitschrift fur Kristallographie* **1975**, *142*, 117−120.
(25) Bersuker, I. B. *Electronic Structure and Properties of Transition Metal Compounds: Introduction to the Theory*; John Wiley & Sons, Inc.: New York, 2010.
(26) Koper, M. T. M. *J. Electroanal. Chem.* **2011**, *660*, 254−260.
(27) Man, I. C.; Su, H. Y.; Calle-Vallejo, F.; Hansen, H. A.; Martinez, J. I.; Inoglu, N. G.; Kitchin, J.; Jaramillo, T. F.; Norskov, J. K.; Rossmeisl, J. *ChemCatChem* **2011**, *3*, 1159−1165.
(28) Vojvodic, A.; Calle-Vallejo, F.; Guo, W.; Wang, S.; Toftelund, A.; Studt, F.; Martinez, J. I.; Shen, J.; Man, I. C.; Rossmeisl, J.; Bligaard, T.; Norskov, J. K.; Abild-Pedersen, F. *J. Chem. Phys.* **2011**, *134*, 244509.
(29) Wang, L. P.; Van Voorhis, T. *J. Phys. Chem. Lett.* **2011**, *2*, 2200−2204.
(30) Wills, A. S.; Raju, N. P.; Greedan, J. E. *Chem. Mater.* **1999**, *11*, 1510−1518.
(31) David, W. I. F.; Thackeray, M. M.; Picciotto, L. A. D.; Goodenough, J. B. *J. Solid State Chem.* **1987**, *67*, 316−323.
(32) Gummow, R. J.; Liles, D. C.; Thackeray, M. M. *Mater. Res. Bull.* **1993**, *28*, 235−246.
(33) Pourbaix, M. *Atlas of Electrochemical Equilibria in Aqueous Solutions*, 2nd ed.; National Association of Corrosion Engineers: Houston, 1974.

DOI: 10.1021/acscatal.5b00265
ACS Catal. 2015, 5, 3403−3410